Nano Energy 35 (2017) 331–340

Contents lists available at ScienceDirect

Nano Energy

journal homepage: www.elsevier.com/locate/nanoen

Communication

Low temperature synthesis of ternary metal phosphides using plasma for asymmetric supercapacitors

Hanfeng Liang, Chuan Xia, Qiu Jiang, Appala N. Gandi, Udo Schwingenschlögl, Husam N. Alshareef*

Materials Science and Engineering, King Abdullah University of Science and Technology (KAUST), Thuwal 23955-6900, Saudi Arabia

ARTICLE INFO

Keywords:
Plasma synthesis
Transition metal phosphides
NiCoP
Asymmetric supercapacitors
Energy storage

ABSTRACT

We report a versatile route for the preparation of metal phosphides using PH_3 plasma for supercapacitor applications. The high reactivity of plasma allows rapid and low temperature conversion of hydroxides into monometallic, bimetallic, or even more complex nanostructured phosphides. These same phosphides are much more difficult to synthesize by conventional methods. Further, we present a general strategy for significantly enhancing the electrochemical performance of monometallic phosphides by substituting extrinsic metal atoms. Using NiCoP as a demonstration, we show that the Co substitution into Ni_2P not only effectively alters the electronic structure and improves the intrinsic reactivity and electrical conductivity, but also stabilizes Ni species when used as supercapacitor electrode materials. As a result, the NiCoP nanosheet electrodes achieve high electrochemical activity and good stability in 1 M KOH electrolyte. More importantly, our assembled NiCoP nanoplates//graphene films asymmetric supercapacitor devices can deliver a high energy density of 32.9 Wh kg^{-1} at a power density of 1301 W kg^{-1}, along with outstanding cycling performance (83% capacity retention after 5000 cycles at 20 A g^{-1}). This activity outperforms most of the NiCo-based materials and renders the NiCoP nanoplates a promising candidate for capacitive storage devices.

1. Introduction

The utilization of sustainable energies such as sunlight and wind holds the promise to fulfil the ever-growing global energy demands of future societies [1,2]. Harvesting energy from these renewable sources requires efficient and affordable energy storage technologies. Supercapacitors, which store energy in terms of charges on electrode surfaces, are now considered as one of the most promising energy storage devices [3–9]. One of the most attractive characteristics of supercapacitors is that they can provide higher energy density than that of traditional capacitors, and greater power density than that of rechargeable batteries, bridging the gap between traditional capacitors and batteries [3–9]. Based on the charge storage mechanism, supercapacitors can be divided into two categories, the electrical double layer capacitors (EDLCs) which accumulate charges by ion adsorption at the electrode/electrolyte interface and pesudocapacitors which chemically store charges via faradaic redox reactions at the surface [3–9]. The latter has attracted intense attention due to their much higher (typically 10–100 times) specific capacitance and energy density compared to that of EDLCs [10,11]. Transition metal-based compounds are popular pesudocapacitors electrode materials because of their multiple valence states that enable fast surface faradaic redox reactions [10,12–18].

Among them, hydroxides and oxides are of particular interest owing to their high theoretical capacitances, earth abundance, and environmental friendliness [10,12–16,19–22]. However, they suffer from poor electrical conductivity. One effective approach to overcome this drawback is to hybridize with highly conductive materials such as graphene [19,21–26]. Another strategy is to improve the conductivity by elemental doping or, searching for new electrode materials that are intrinsically more conductive. From this perspective, metallic transition metal sulfides, selenides, and phosphides should be promising candidates [27,28]. Indeed, several sulfides and selenides have been explored as new electroactive materials for supercapacitors and often show superior performance than oxides and hydroxides [29–31]. Besides, metal phosphides also exhibit promising electrochemical properties and have been widely employed as electrocatalysts and lithium-ion battery electrodes [28,32–34]. Unexpectedly, however, the use of metal phosphides for supercapacitors is still quite limited. We noticed that there are only a few reports on Ni-P for supercapacitors [35–38], which show that the Ni-P can deliver high specific capacity (we use capacity here because Ni and Co based compounds are

* Corresponding author.
E-mail address: husam.alshareef@kaust.edu.sa (H.N. Alshareef).

http://dx.doi.org/10.1016/j.nanoen.2017.04.007
Received 29 January 2017; Received in revised form 2 April 2017; Accepted 3 April 2017
Available online 06 April 2017
2211-2855/ © 2017 Elsevier Ltd. All rights reserved.

recognized as battery-type materials [39]) but with poor rate capability and cycling performance. This phenomenon is commonly seen for Ni-based materials [20,40–43], possibly due to the poor structural stability during the fast charge-discharge process. On the other hand, Co-based compounds possess excellent stability even though their specific capacity is relatively low [44–46]. Further, bimetallic NiCo compounds show richer faradaic redox reactions, higher electrical conductivity and stability, thus often result in enhanced electrochemical performance than their corresponding single metal counterparts, as already demonstrated for NiCo oxides and chalcogenides [29–31,47]. Encouraged by these findings, we predicted that the electrochemical activity and stability of nickel phosphides could be dramatically improved through Co substitution.

Herein we report a promising approach toward enhancing the electrochemical performance of monometallic phosphides as supercapacitor electrodes through extrinsic metal substitution. Using NiCoP as a demonstration, we showed that Co incorporation into Ni_2P doesn't change the crystal structure (both the Ni_2P and NiCoP adopt the hexagonal Fe_2P structure, see Fig. S1 in the Supporting Information), but effectively tunes the electronic structure and the intrinsic reactivity and electrical conductivity. Compared to Ni_2P and CoP, the bimetallic NiCoP exhibits superior electrochemical performance in terms of high specific capacity and good cycling performance. Furthermore, the asymmetric supercapacitor devices based on NiCoP nanoplates and graphene films can deliver a high energy density of 32.9 Wh kg^{-1} at a power density of 1301 W kg^{-1}, along with outstanding cycling performance (83% capacity retention after 5000 cycles at 20 A g^{-1}). This result outperforms most of the NiCo-based materials, indicating that NiCoP nanoplates are promising candidates for energy storage devices.

2. Experimental section

2.1. Synthesis of hydroxides precursor

Carbon paper substrate was treated by annealing in air at 700 °C for 10 min to improve the surface hydrophilicity before use. Then NiCo hydroxide nanoplates were synthesized by a hydrothermal method. In a typical synthesis, 2.5 mmol of $Ni(NO_3)_2{\cdot}6H_2O$, 2.5 mmol of $Co(NO_3)_2{\cdot}6H_2O$, and 10 mmol of hexamethylenetetramine (HMT) were dissolved in 30 mL of distilled water, which was then transferred to a 50 mL autoclave containing the carbon paper substrate (typically 2×5 cm). The autoclave was sealed and heated at 100 °C for 10 h. After cooling, the substrate was removed, rinsed with ethanol and water, and dried under a flow of nitrogen gas. The Ni and Co hydroxides were synthesized using the same procedure as that of NiCo hydroxide, except 5 mmol $Ni(NO_3)_2{\cdot}6H_2O$ or $Co(NO_3)_2{\cdot}6H_2O$ instead of 2.5 mmol of $Ni(NO_3)_2{\cdot}6H_2O$ and 2.5 mmol of $Co(NO_3)_2{\cdot}6H_2O$ was used.

2.2. Conversion of hydroxides to phosphides

The carbon paper substrate (typically 0.5×2 cm) covered with hydroxides was placed in the chamber of a plasma-enhanced chemical vapor deposition (PECVD) system, followed by thermal phosphorization at 250 °C for 15 min using PH_3 plasma. The conditions for the plasma treatment were PH_3/He (5:95 volumetric ratio) flux of 50 sccm, a base pressure of 980 mTorr, and a power of 100 W.

2.3. Structural characterization

The as-synthesized samples on carbon paper were characterized using a Bruker D8 ADVANCE X-ray diffractometer (XRD) using Cu Kα radiation (λ=1.5406 Å), a FEI Nova Nano 630 scanning electron microscope (SEM), and a FEI Titan 80–300 ST (300 kV) transmission electron microscope (TEM) with energy dispersive X-ray spectroscopy (EDS) capabilities. Note that the XRD patterns were taken on the powder scraped off the carbon paper substrate. The electron energy-loss spectroscopy (EELS) analyses were performed under the aberration corrected scanning TEM (STEM) mode. The Ni-L23 (855 eV), Fe-L23 (710 eV), and P-L23 (132 eV) energy loss edges were selected to generate the Ni, Fe, and P maps, respectively. X-ray photoelectron spectroscopy (XPS) measurements were performed using a Kratos Axis Ultra DLD spectrometer with Al Kα radiation ($h\nu$ =1486.6 eV). All XPS spectra were calibrated by shifting the detected adventitious carbon C 1 s peak to 284.4 eV.

2.4. Electrical conductivity measurements of individual phosphide nanoplates

The phosphide nanoplates grown on carbon paper were immersed into ethanol and sonicated for 30 min. Then a few drops of the suspension were casted onto Si/SiO_2 (280 nm) wafers. Afterwards, the Ti (10 nm)/Au (100 nm) electrodes for transport tests were fabricated on the high-quality samples (flat and large nanoplates) using standard e-beam lithography (EBL) and e-beam evaporation. The transport properties of as-made nanodevices were analyzed by Keithley 4200 semiconductor characterization system.

2.5. Electrochemical measurements

The electrochemical measurements were carried out at room temperature in both three-electrode (half-cell) and two-electrode (full cell) configurations. In the half-cell measurements, the NiCoP on carbon paper was directly used as the working electrode without adding any extra binders or conductive additives, a Pt wire and a Ag/AgCl electrode were used as the counter and reference electrodes, respectively. Whereas in the full cell measurements, a carbon paper with NiCoP nanoplates grown on it and a graphene film were used as the positive and negative electrodes respectively with a porous polymer membrane (Celgrad 3501) as the separator to assemble a coin cell. Prior to the fabrication of the asymmetric supercapacitors, the mass of the positive and negative electrodes was balanced according to the following equation:

$$\frac{m_+}{m_-} = \frac{C_{s-}\cdot\Delta V_-}{C_{s+}\cdot\Delta V_+} \quad (1)$$

where m is the mass, C_s is the specific capacitance and ΔV is the voltage range for positive (+) and negative (-) electrodes, respectively. For a typical device, the total mass loading is ~3.4 mg cm^{-2} with a stack thickness of ~0.8 mm. For all measurements, 1 M KOH aqueous solution was used as electrolyte. Cyclic voltammetry, galvanostatic charge-discharge tests, and electrochemical impedance spectroscopy (EIS) measurements were conducted on a Bio-Logic VMP3 potentiostat. EIS tests were performed at open circuit voltage in the frequency range of 100 kHz–0.01 Hz at an amplitude of 5 mV.

2.6. Calculations

The capacities were calculated from the galvanostatic charge-discharge curves. For the half cell, the specific capacity (C_s, mAh g^{-1}) was calculated according to

$$C_s = \frac{2i\int V dt}{mV} \quad (2)$$

whereas for the full cell, the cell capacity (C_c, mAh g^{-1}) was calculated according to

$$C_{cell} = \frac{2i\int V dt}{MV} \quad (3)$$

where i (A) is the current density, t (s) the discharge time, V (V) the potential window, m (g) the mass of the active materials on the single electrodes, and M (g) the total mass of the active materials on both the

positive and negative electrodes. The energy density (E, Wh kg^{-1}) and power density (P, W kg^{-1}) are given by:

$$E = \frac{i\int V dt}{M \times 3.6} \quad (4)$$

$$P = \frac{E}{t} \times 3600 \quad (5)$$

2.7. Computational methodology

We evaluate the electronic band structure of NiCoP, Ni_2P, and CoP using the Vienna Ab-initio Simulation Package [48]. Nine, ten, and five valence electrons of Co, Ni, and P, respectively, are considered and plane waves with kinetic energies up to 300 eV are taken into account in the expansion of the electronic wave functions. The generalized gradient approximation of the exchange-correlation potential in the Perdew-Burke-Ernzerhof flavor is employed and the tetrahedron method with Blöchl corrections is used for Brillouin zone integrations [49]. NiCoP and Ni_2P have hexagonal symmetry (space group 189), while CoP has orthorhombic symmetry (space group 62). Structure optimizations are performed on Γ-centered k-meshes (12×12×20 for NiCoP and Ni_2P, 12×18×10 for CoP). Finer k-meshes are used in the density of states calculations (16×16×26 for NiCoP and Ni_2P, 18×28×16 for CoP).

3. Results and discussion

We first synthesized Ni_2P and CoP porous nanoplates on carbon paper by converting the corresponding hydroxide precursors using our recently developed PH_3 plasma-assisted method (Fig. 1) [50]. Compared to the conventional methods for the preparation of metal phosphides [34], our developed plasma route allows direct conversion of metal hydroxides into phosphides at low temperature and in a rapid manner, and more importantly, could serve as a versatile route to synthesize nanostructured complex phosphides that otherwise are not easy to prepare. The morphology of the samples was characterized by scanning electron microscopy (SEM) and transmission electron microscopy (TEM). It can be seen that Ni_2P nanoplates with high density are uniformly grown on carbon paper substrate (Fig. S2a, Supporting Information). These nanoplates are interconnected with each other, forming a relatively open 3D structure (inset of Fig. 2a). TEM observation reveals that the nanoplates are composed of many small nanocrystallites (Fig. 2a). The polycrystalline nature is further confirmed by the selected area electron diffraction (SAED) pattern (Fig. 2b), which can be indexed into hexagonal Ni_2P. Fig. 2c shows a typical high-resolution TEM (HRTEM) image of the Ni_2P nanoplates. The lattice spacing of 0.34 nm corresponds to the (001) planes of Ni_2P (Fig. 2c). The molar ratio of Ni:P is determined to be 2.14:1 based on the electron dispersive spectroscopy (EDS) analysis (Fig. S2b, Supporting Information), which is close to the stoichiometric ratio of Ni_2P. We further carried out the X-ray photoelectron spectroscopy (XPS) to probe the surface compositions and chemical states. The Ni 2p spectrum presents two peaks with binding energies of 853.3 ($2p_{3/2}$) and 870.7 eV ($2p_{3/2}$), respectively, which are the characteristic of Ni-P ($Ni^{\delta+}$) bonding from phosphides (Fig. S2c, Supporting Information) [51,52]. Whereas for the P 2p spectrum, two main peaks appear at 129.4 and 133.6 eV, corresponding to the reduced phosphorous ($P^{\delta-}$) in the form of metal phosphides (i.e. Ni_2P) and the phosphate species (P^{5+}), respectively (Fig. S2d, Supporting Information).[51,52] The presence of characteristic XPS peaks, together with the HRTEM, SAED, and EDS results shown above, suggest the formation of Ni_2P after the plasma conversion. Similar to Ni_2P, the CoP after conversion of is found to consist of porous nanoplates (Fig. S3a, Supporting Information and Fig. 2d). The SAED pattern reveals that the as-converted product is polycrystalline and can be indexed into orthorhombic CoP (Fig. 2e). The lattice spacing of 0.28 nm corresponds to the (002) planes of CoP (Fig. 2f). EDS (Fig. S3b, Supporting Information) and XPS (Fig. S3c and d, Supporting Information) analyses further confirm the formation of CoP.

We then performed the electrochemical measurements on the plasma converted Ni_2P and CoP using three-electrode configuration in 1 M KOH. The cyclic voltammetry (CV) curves of Ni_2P at different scan rates show a pair of redox peaks, corresponding to the well-documented Ni^{2+}/Ni^{3+} redox process (Fig. S4a). The nonlinear galvanostatic charge-discharge (GCD) profiles further suggest the faradaic process (Fig. S4b). It is worth mentioning that the CV curve at low scan rate shows three distinct oxidation peaks (Fig. S5a). The peak at 0.44 and 0.5 V vs Ag/AgCl can be assigned to the oxidation of Ni_2P ($Ni^{\delta+}$) into β-$Ni(OH)_2$ (Eq. (6)) and β-$Ni(OH)_2$ into β-NiOOH (Eq. (7)). Note that the β-NiOOH can be converted into γ-NiOOH upon slow, irreversible overcharging during cycling in KOH [53]. This phenomenon was originally reported by Bode et al. [54]. Therefore, the peak at 0.6 V vs Ag/AgCl is due to the formation of γ-NiOOH. The conversion

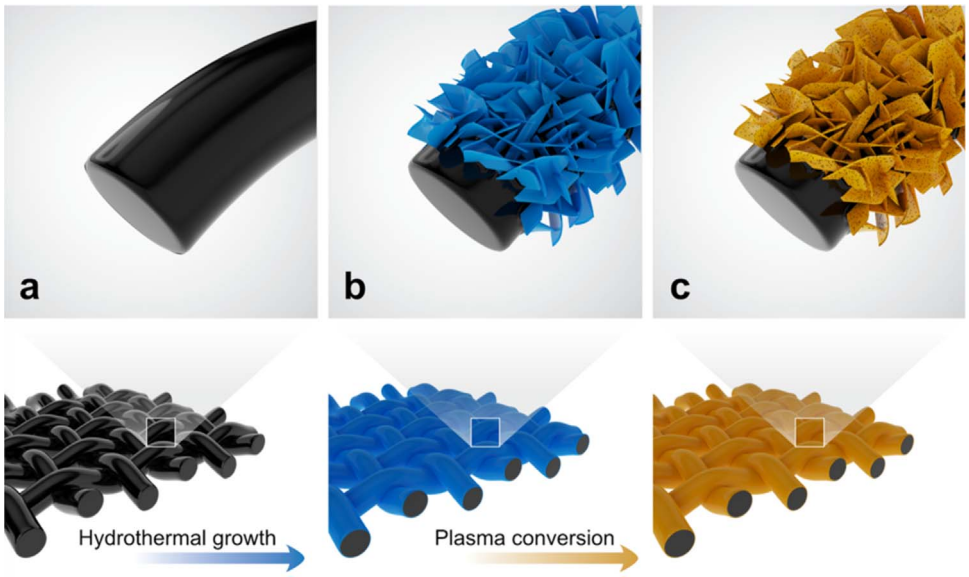

Fig. 1. Schematic illustration of the synthetic process of metal phosphide nanostructures. (a) Carbon paper substrate. (b) Hydrothermal growth of metal hydroxide nanoplates precursor on carbon paper. (c) Plasma conversion of hydroxide nanoplates into phosphide porous nanoplates.

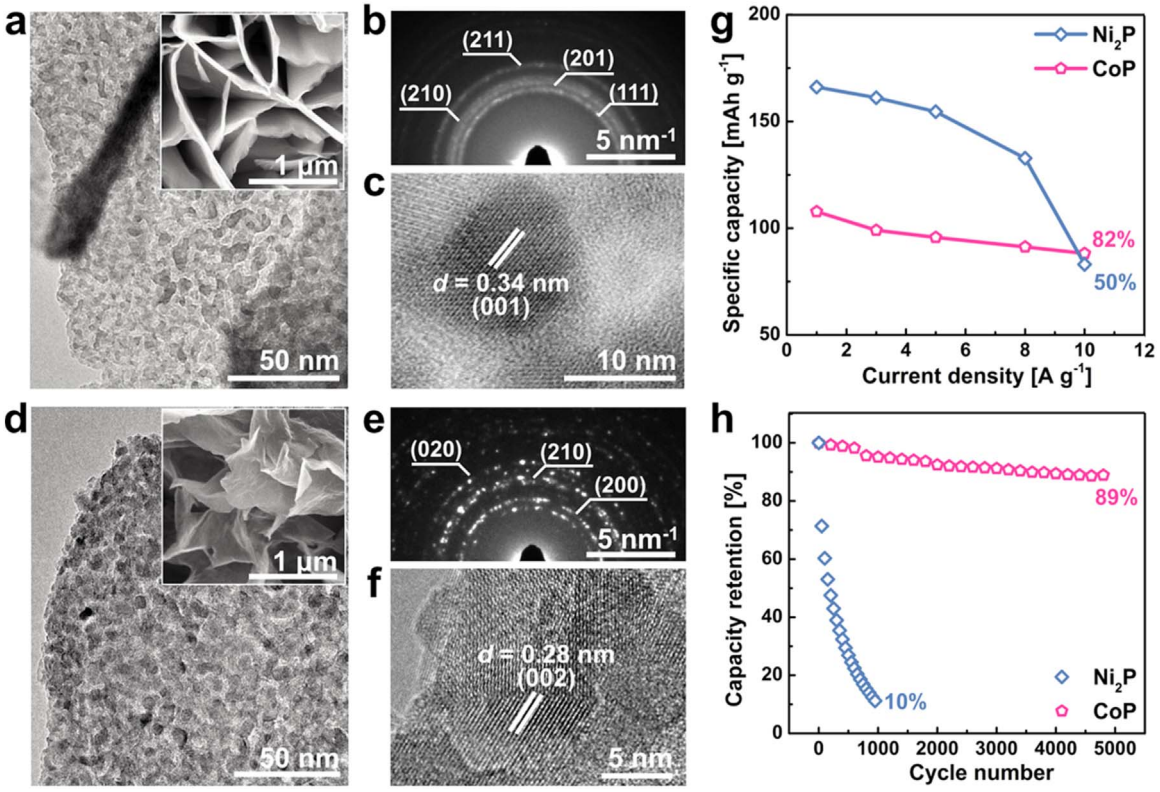

Fig. 2. Structures and electrochemical properties of Ni and Co phosphides. (a) TEM image, (b) SAED pattern and (c) HRTEM image of Ni_2P nanoplates. (d) TEM image, (e) SAED pattern, and (f) HRTEM image of CoP nanoplates. (g) Comparison on the specific capacity of the Ni_2P and CoP. (h) Comparison on cycling stability of the Ni_2P and CoP.

of β-NiOOH to γ-NiOOH is associated with a large volume expansion (44%), which leads to a mechanical deformation and thus results in an irreversible damage to the electrode [55–57]. This phase transformation partially explains the poor stability of Ni_2P as demonstrated later in Fig. 2h.

$$Ni^{\delta+} + 2\ OH^- \rightarrow Ni(OH)_2 + (2\text{-}\delta)\ e^- \quad (6)$$

$$\beta\text{-}Ni(OH)_2 + OH^- \longleftrightarrow \beta\text{-}NiOOH + H_2O + e^- \quad (7)$$

Whereas for CoP electrodes, the CV curves (Fig. S4c) and the GCD profiles (Fig. S4d) clearly indicate the faradaic processes. The CV curve recorded at 1 mV s^{-1} shows one small oxidation peak at −0.02 V vs Ag/AgCl and two pronounced anodic peaks at 0.08 and 0.48 V vs Ag/AgCl, respectively (Fig. S5b). The former corresponds to the oxidation of CoP ($Co^{\delta+}$) into $Co(OH)_2$ (Eq. (8)), whereas the latter two can be assigned to the transformation process of $Co(OH)_2$ into CoOOH (Eq. (9)) and the subsequent CoOOH into CoO_2 (Eq. (10)), respectively [44].

$$Co^{\delta+} + 2\ OH^- \rightarrow Co(OH)_2 + (2\text{-}\delta)\ e^- \quad (8)$$

$$Co(OH)_2 + OH^- \longleftrightarrow CoOOH + H_2O + e^- \quad (9)$$

$$CoOOH + OH^- \longleftrightarrow CoO_2 + H_2O + e^- \quad (10)$$

We then compared the specific capacity of Ni_2P and CoP. Note that it has been demonstrated recently that for those faradaic electroactive materials (e.g., Ni and Co based compounds) that exhibit battery-type nonlinear GCD profiles in alkaline electrolytes, the energy storage performance should be described as specific capacity (mAh g^{-1}) to distinguish from true pseudocapacitive electrode materials such as RuO_2 and MnO_2 [39]. As shown in Fig. 2g, the Ni_2P delivers a high specific capacity of 166 mAh g^{-1} at 1 A g^{-1}, however, it decades quickly and only 50% of the capacity is maintained at 10 A g^{-1}. In comparison, a high capacity retention of 82% is achieved for CoP though it exhibits a relatively low specific capacity of 108 mAh g^{-1} at 1 A g^{-1}. The CoP also shows better stability than Ni_2P. The capacity retention is as high as 89% after 5000 cycles even at a high discharge current density of 10 A g^{-1} (Fig. 2h). Whereas, the capacity of Ni_2P rapidly drops to 10% of the initial value after 1000 cycles, suggesting the poor stability (Fig. 2h). Such poor rate performance is commonly seen for Ni-based compounds [20,40–43]. For both the Ni_2P and CoP, the morphology doesn't show significant changes (Fig. S6). However, the XPS analysis clearly demonstrates that the surface composition has been changed. The binding energy of 855.5 eV for Ni $2p_{3/2}$ suggests the presence of Ni^{2+} and Ni^{3+} species after cycling (Fig. S7) [58]. Whereas for CoP, the Co $2p_{3/2}$ peak located at 780.0 eV can be assigned to the CoOOH [59]. These results suggest that the surface of the phosphide materials is oxidized during the electrochemical measurements and are in agreement with the CV tests.

We noted that the Ni_2P possesses a high specific capacity though the rate capability is quite poor, whereas the CoP has a relatively low capacity but good rate capability. Further, the oxidation potential of $Co^{\delta+}/Co^{2+}$ is lower than that of $Ni^{\delta+}/Ni^{2+}$(see Fig. S5), which means that for a NiCo bimetallic phosphide the $Co(OH)_2$ would be formed before $Ni^{\delta+}$ being oxidized into $Ni(OH)_2$ during cycling, and may consequently serve as a surface protective layer that alleviates the damage caused by the phase transformation of β-NiOOH to γ-NiOOH. Encouraged by these findings, we hypothesized that the electrochemical activity and stability of Ni_2P could be dramatically enhanced through Co substitution. We hence set out to synthesize a bimetallic phosphide, namely NiCoP, which we expected to inherit the high capacity of Ni_2P and the good stability of CoP. The NiCoP was converted from NiCo hydroxide precursor using plasma. The powder X-ray diffraction (PXRD) pattern (Fig. 3a) clearly confirms the formation of hexagonal NiCoP (space group $P\text{–}62m$, a =5.834 Å). EDS analysis reveals that the atomic ratio of Ni:Co:P is 1.1:1:1.1, close to the stoichiometric ratio of NiCoP (Fig. S8). The morphology was then characterized by SEM and TEM. Similar to Ni_2P and CoP, the NiCoP also exhibits a hierarchical structure with nanoplates lying aslant or perpendicular to the substrate (Fig. 3b and c). TEM image further shows that many nanopores are

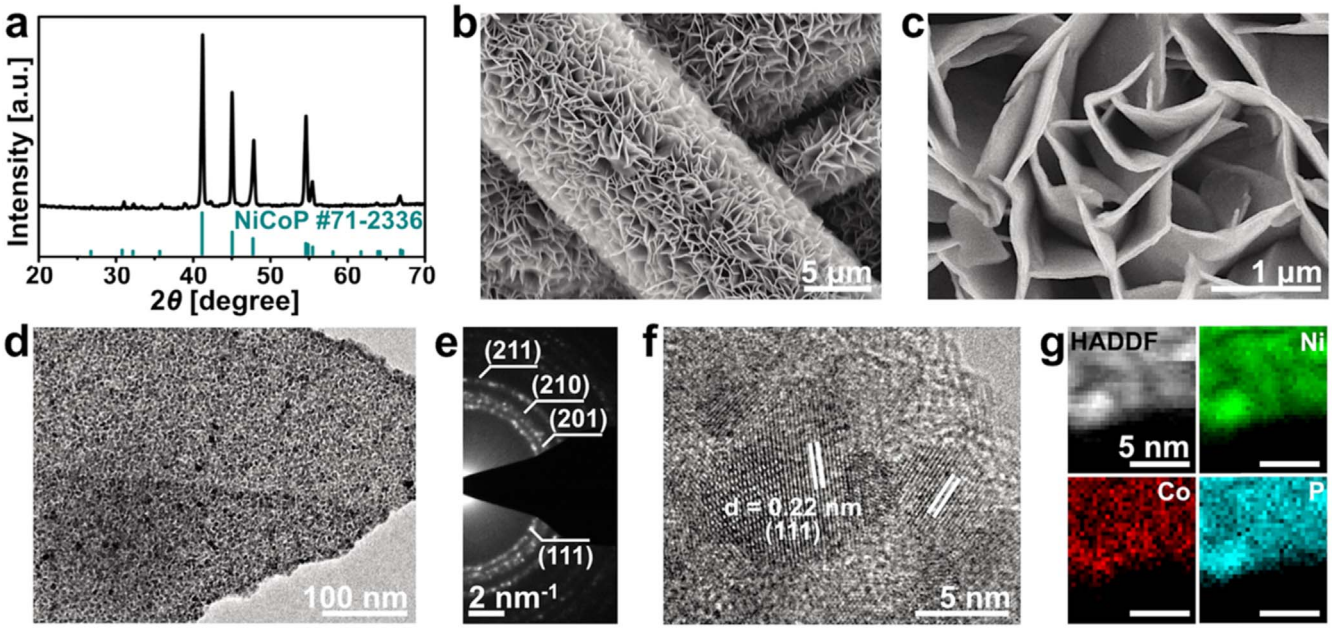

Fig. 3. Characterization of the as-converted NiCoP nanoplates. (a) PXRD pattern of the NiCoP nanoplates powder scraped from the carbon paper. (b, c) SEM images of the NiCoP nanoplates on carbon paper substrate. (d) TEM image, (e) corresponding SAED pattern, (f) HRTEM image, and (g) STEM-EELS elemental maps of the NiCoP nanoplates.

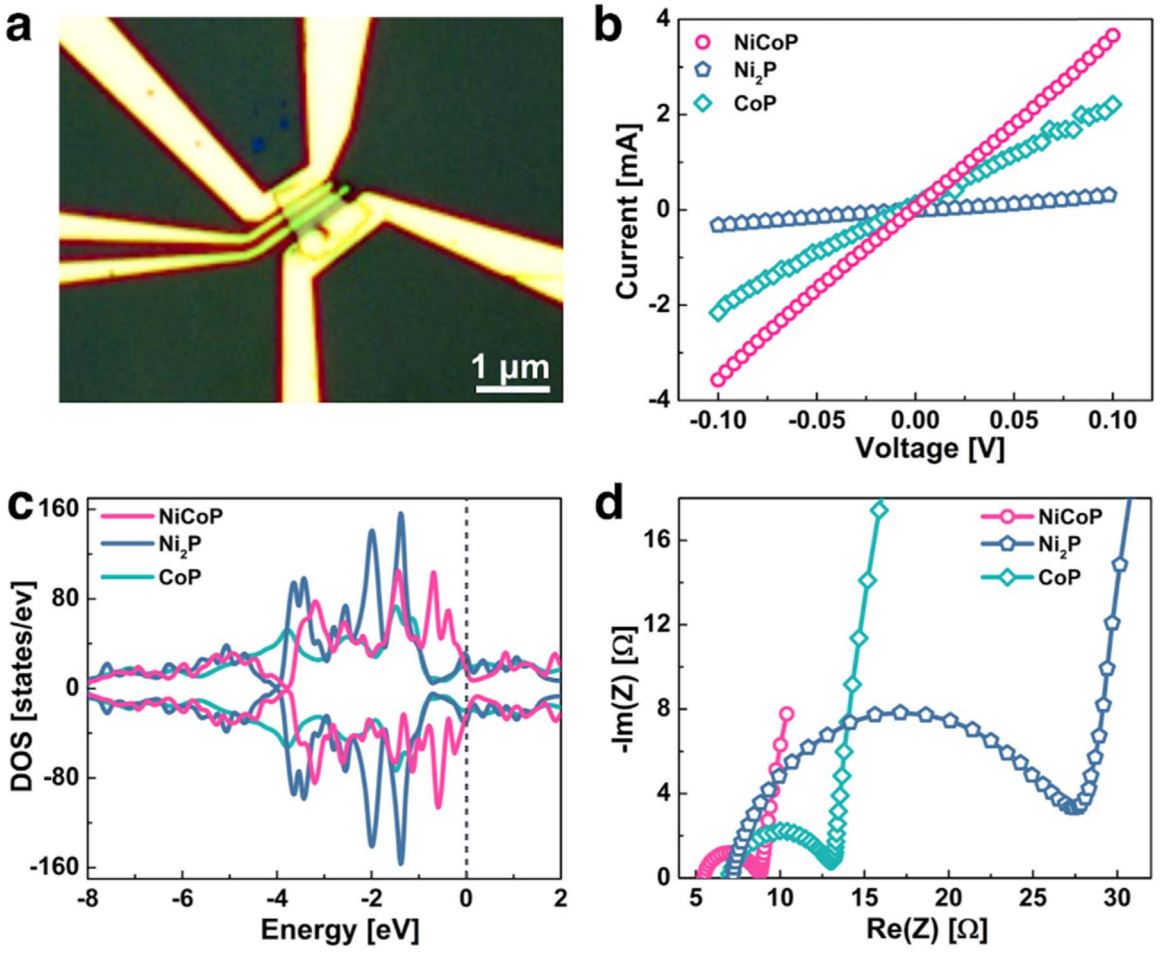

Fig. 4. (a) Optical micrograph of a phosphide nanoplate device with four-probe geometry for resistivity measurements. The yellow shaded area shows the electrodes. (b) *I-V* characteristics of NiCoP, Ni_2P and CoP single nanoplates measured at room temperature. (c) Projected densities of states for NiCoP, Ni_2P, and CoP. (d) Nyquist plots of NiCoP, Ni_2P, and CoP electrodes.

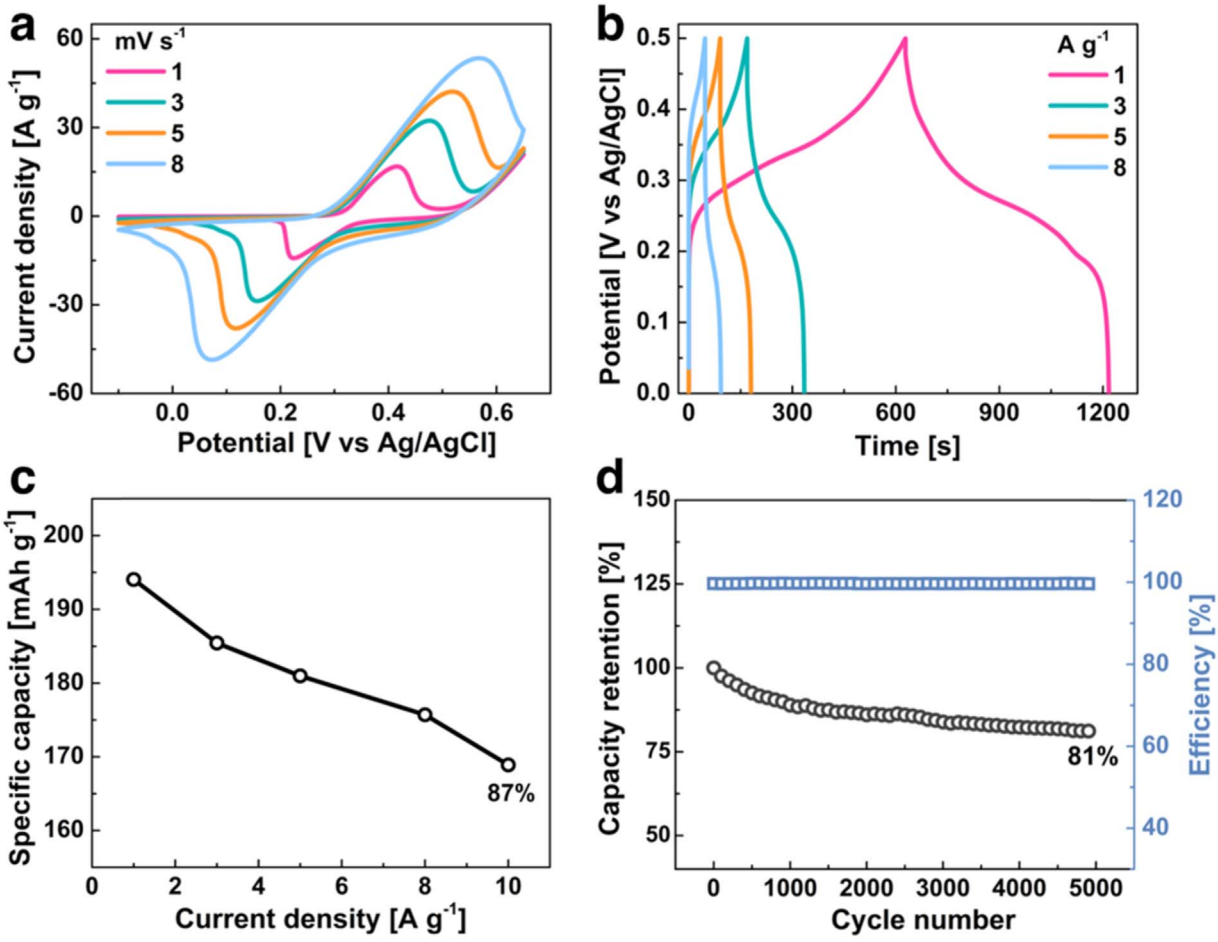

Fig. 5. Electrochemical performance of NiCoP for supercapacitors. (a) CV curves at different scan rates. (b) GCD profiles at different current densities. (c) Specific capacity. (d) Cycling performance at a constant current density of 10 A g^{-1}.

distributed uniformly throughout the NiCoP nanoplates (Fig. 3d). The formation of pores is probably due to the large strain caused by the crystal mismatch, which is commonly observed for materials after phase conversion, e.g., porous $NiSe_2$ nanoplates converted from β-$Ni(OH)_2$ [60]. Such porous nanostructure could possibly offer high electrode/electrolyte interface area, and thus promote the electrochemical performance [47]. The SAED pattern indicates the polycrystalline nature of the product and can be indexed into the hexagonal NiCoP (Fig. 3e), in agreement with the PXRD result. Fig. 3f shows a typical HRTEM image, wherein the lattice spacing is measured to be 0.22 nm, consistent with the *d*-spacing of the (111) planes of NiCoP (Fig. 3f). The presence of Ni, Co, and P is further confirmed by the scanning transmission electron microscopy-electron energy loss spectroscopy (STEM-EELS) elemental mapping (Fig. 3g). The formation of NiCoP after plasma treatment is further confirmed by the XPS analysis (Fig. S9). These results unambiguously demonstrate that the plasma-assisted conversion could serve as an effective and versatile route to prepare monometallic, bimetallic, or even more complex phosphides that otherwise are much more difficult to synthesize.

As we mentioned earlier, both Ni_2P and NiCoP adopt the hexagonal Fe_2P structure (see Fig. S1). Such similarity allows the smooth substitution of Co into Ni_2P without significantly changing the crystal structure. However, the Co substitution alters the electronic structure of Ni_2P and thus the conductivity and reactivity. Theoretical calculation shows that Ni_2P, CoP, and NiCoP have no band gap (metallic character, Fig. S10). We then measured the resistivities of individual nanoplates of these phosphide materials at room temperature (Fig. 4a). All samples exhibit liner *I-V* characteristics indicative of ohmic contact behavior as shown in Fig. 4b. The resistivity of NiCoP (1.1×10^3 μΩ cm) is much lower than that of CoP (2.7×10^3 μΩ cm) and Ni_2P (4.1×10^3 μΩ cm), suggesting that the electrical conductivity of Ni_2P is improved after Co substitution. Further, calculated densities of states show the d-states of NiCoP closer to the Fermi level (Fig. 4c), which implies that NiCoP is intrinsically more reactive and likely possesses a better electrochemical activity than Ni_2P and CoP. We further carried out the electrochemical impedance spectroscopy (EIS) measurements in the frequency range of 100 kHz–0.01 Hz at 5 mV amplitude. As shown in Fig. 4d, the Nyquist plots for all three materials are composed of one depressed semicircle at high frequencies and a straight line at low frequencies, which are associated with the charge transfer resistance and the mass transfer resistance, respectively. Apparently, the NiCoP electrode shows the lowest equivalent series resistances of around 5 Ω, further demonstrating its highest electrical conductivity. The radius of the semicircle for Ni_2P is much bigger than that of CoP and NiCoP, suggesting the highest charge transfer resistance among the three materials, which further explains the poor rate capability as observed in Fig. 2g. In contrast, the smaller radius of the semicircle and the shorter low-frequency sloping line for NiCoP indicate that the NiCoP has much lower charge and mass transfer resistances. These results demonstrate that the Co substitution could dramatically lower the electronic and ionic resistances of Ni_2P, and therefore lead to a better electrochemical performance.

We then assessed the electrochemical performance of NiCoP nanoplates as positive electrode for supercapacitors using three-electrode configuration in 1 M KOH. Fig. 5a shows the CV curves at various scan rates. A couple of redox peaks associating with the faradaic processes of $Ni^{\delta+}/Ni^{3+}$(see Eqs. (6) and (7)) and $Co^{\delta+}/Co^{4+}$(see Eqs. (8)–(10)) for all CV curves is clearly seen, which implies that the main contribution to the capacity of NiCoP comes from the

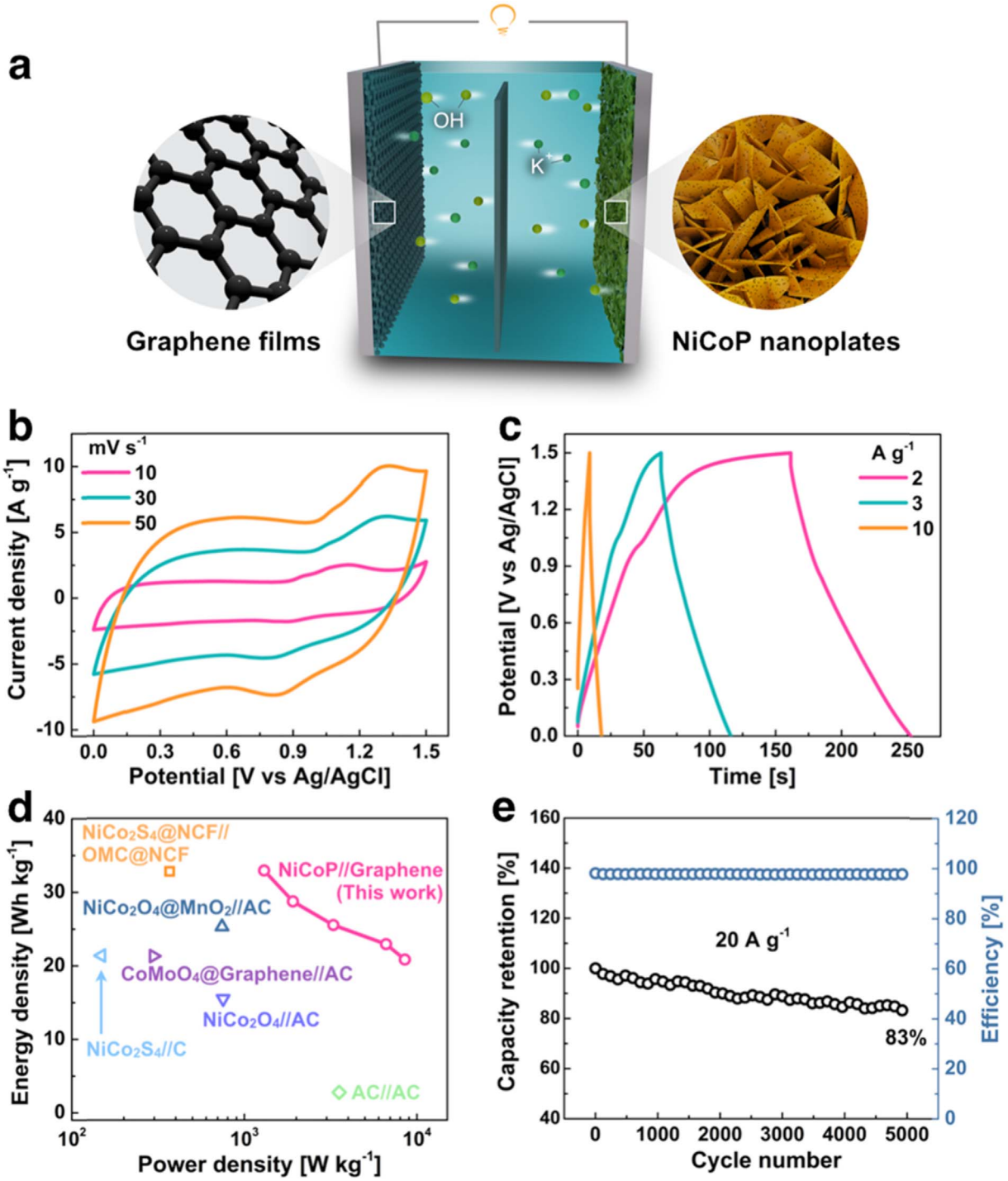

Fig. 6. Electrochemical performance of NiCoP//Graphene asymmetric supercapacitors. (a) Schematic illustration of the asymmetric supercapacitors. (b) CV curves at different scan rates. (c) GCD profiles at different current densities. (d) Ragone plot related to energy and power densities. (e) Cycling performance at a constant current density of 20 A g^{-1}. References cited in d: $NiCo_2S_4$@NCF//OMC@NCF [29], $NiCo_2O_4$@MnO_2//AC [63], $CoMoO_4$@Graphene//AC [64], $NiCo_2O_4$//AC [65], $NiCo_2S_4$//C [66], AC//AC [64]. Note: NCF, N-doped carbon foams; OMC, ordered mesoporous carbon; AC, activated carbon.

faradaic reactions. The potential plateaus in the non-linear GCD profiles are related to the typical faradaic reactions (Fig. 5b), consistent with the electrochemical behavior of the CV curves. The highly symmetric characteristic of the GCD curves and the very small voltage drops observed upon discharging suggest the good electric and ionic conductivity of the NiCoP, in agreement with the EIS result (Fig. 4d). We further calculated the specific capacity of the NiCoP. As summarized in Fig. 5c, the NiCoP electrodes can deliver a high specific capacity of 194 mAh g^{-1} at 1 A g^{-1}. We noted that this value is even higher than that of Ni_2P (166 mAh g^{-1}), which may be due to the intrinsically higher reactivity of the NiCoP as we demonstrated earlier in Fig. 4c. The capacity of NiCoP gradually decreases as the discharge current density increases and finally a specific capacity of 169 mAh g^{-1} is achieved at 10 A g^{-1}, that is, 87% of initial capacity is retained, compared to 50% retention of Ni_2P from 1 to 10 A g^{-1} (see Fig. 2g), suggesting the rate capability of Ni_2P is greatly improved through Co substitution. Furthermore, compared to Ni_2P, the NiCoP also shows significantly enhanced stability upon long term cycling tests. For Ni_2P,

only 10% of the initial capacity is maintained after 1000 cycles at 10 A g^{-1} (Fig. 2h). In sharp contrast, 81% of the initial capacity is maintained for NiCoP after 5000 cycles under the same current density. The SEM images reveal that after cycling, the overall morphology of NiCoP doesn't change much. However, many nanoparticles are found on the initial smooth surface of the nanoplates. We thus carried out the XPS measurements to further understand the surface composition change. Similar to Ni_2P and CoP, after cycling, the XPS peaks associated with the low-valent $Ni^{\delta+}$, $Co^{\delta+}$, and $P^{\delta-}$ as observed in the freshly made NiCoP disappear, indicating the surface of NiCoP has been oxidized. The binding energy of 780.0 eV for Co $2p_{3/2}$ peak is the same as we observed for the CoP after cycling, which can be assigned to the Co^{3+} species (CoOOH) [59]. Whereas the binding energy for Ni $2p_{3/2}$ is 855.8 eV, suggesting the Ni species mainly exist as $Ni(OH)_2$ [61]. Of note, the Ni $2p_{3/2}$ spectrum reveals that for Ni_2P, both Ni^{2+} and Ni^{3+} species are identified after cycling. The XPS analysis confirms our hypothesis that the Co hydroxides could possibly serve as a surface protective layer that prevents Ni from being oxidized to some degree, and thus improve the overall stability of the NiCoP. These results prove the efficacy of significantly enhancing the electrochemical performance and stability of Ni_2P through Co substitution and further establish our NiCoP nanoplates as a promising electrode material for supercapacitors.

Given the potential of the NiCoP nanoplates as supercapacitor electrode materials, we further assembled asymmetric supercapacitor devices using NiCoP nanoplates and graphene films as the positive and negative electrodes, respectively (Fig. 6a). The graphene films were synthesized using an established procedure [62] and can deliver a high specific capacitance (222 F g^{-1} at 1 A g^{-1}) along with outstanding rate capability (Fig. S13) in 1 M KOH. To achieve the optimal performance of the asymmetric supercapacitors, the mass loadings of the two electrodes were balanced based on the voltage windows and the specific capacitances (or capacities) of the electrode materials (see details in experimental section). Fig. 6b shows the CV curves recorded at different scan rates within the potential range of 0–1.5 V. The CV curves exhibit quasi-rectangular shapes with distinguished redox peaks, a typical hybrid capacitive behavior. Moreover, the shapes are almost the same even at high scan rates, suggesting the good rate capability of the NiCoP//graphene films devices. We further carried out the GCD measurements under different current densities and the GCD profiles are shown in Fig. 6c. The nearly symmetric charge-discharge curves indicate a high columbic efficiency. Of note, these sloped voltage profiles are the typical feature of pseudocapacitive charge storage, in agreement with the CV tests. The specific cell capacities were calculated based on the GCD curves. Impressively, the asymmetric devices can deliver a high cell capacity of 43.8 mAh g^{-1} at 2 A g^{-1}, corresponding to an areal capacity of 148.9 μAh cm^{-2} at 6.8 mA cm^{-2} (Fig. S14). Moreover, the devices still maintain 28 mAh g^{-1} (94.2 μAh cm^{-2}) at a high current density of 10 A g^{-1} (34 mA cm^{-2}) with a capacity retention of 64%. We further examined the energy density and the power density of the NiCoP//graphene films asymmetric devices and the result is presented as the Ragone plot in Fig. 6d. Strikingly, the asymmetric devices achieve a high energy density of 32.9 Wh kg^{-1}, corresponding to a stack energy density of 1.4 mWh cm^{-3} at a power density of 1301 W kg^{-1} (55.3 mW cm^{-3}) and can still remain 20.8 Wh kg^{-1} (0.89 mWh cm^{-3}) at 8509 W kg^{-1} (361.6 mW cm^{-3}). These numbers are much better than those reported for NiCo-based and many other high-performance asymmetric supercapacitors (see comparison in Fig. 6d). Besides the high energy and power densities achieved, our NiCoP//graphene films asymmetric supercapacitor devices also showed quite good cycling performance. 83% capacity retention is reached after 5000 cycles even at a high discharge current density of 20 A g^{-1} (Fig. 6e). These results establish the NiCoP nanosheet arrays as a promising supercapacitor electrode material and our developed NiCoP//graphene films asymmetric supercapacitors as a potential energy storage device.

4. Conclusions

In summary, we have developed a PH_3 plasma-assisted route for preparing ternary NiCoP nanoplates at low temperature and further explored their applications in asymmetric supercapacitors. We showed that the electrochemical activity and stability of Ni_2P can be significantly enhanced after Co substitution. The resultant NiCoP nanoplates inherit the high capacity of Ni_2P and the good rate capability of CoP when used as supercapacitor electrodes. More importantly, when assembled together with graphene films, the asymmetric supercapacitor devices can deliver a high energy density of 32.9 Wh kg^{-1} at a power density of 1301 W kg^{-1} along with outstanding cycling performance, which is superior than most of the NiCo-based asymmetric devices reported so far. Our results suggest that substituting extrinsic metal atoms could serve as a general strategy for tuning the reactivity and consequently enhancing the electrochemical performance of transition metal phosphides. Further, the plasma-assisted route can be generally applied to synthesize various nanostructured metal phosphides for various applications.

Acknowledgements

Research reported in this publication was supported by King Abdullah University of Science and Technology (KAUST). Figs. 1 and 6a were produced by Ivan Gromicho, scientific illustrator at KAUST.

Appendix A. Supporting information

Supplementary data associated with this article can be found in the online version at doi:10.1016/j.nanoen.2017.04.007.

References

[1] M. Dresselhaus, I. Thomas, Alternative energy technologies, Nature 414 (2001) 332–337.
[2] J.P. Holdren, Energy and sustainability, Science 315 (2007) 737-737.
[3] P. Simon, Y. Gogotsi, Materials for electrochemical capacitors, Nat. Mater. 7 (2008) 845–854.
[4] A.S. Arico, P. Bruce, B. Scrosati, J.-M. Tarascon, W. Van Schalkwijk, Nanostructured materials for advanced energy conversion and storage devices, Nat. Mater. 4 (2005) 366–377.
[5] A. Vlad, N. Singh, C. Galande, P.M. Ajayan, Design considerations for unconventional electrochemical energy storage architectures, Adv. Energy Mater. 5 (2015).
[6] M. Winter, R.J. Brodd, What are batteries, fuel cells, and supercapacitors?, Chem. Rev. 104 (2004) 4245–4270.
[7] G. Wang, L. Zhang, J. Zhang, A review of electrode materials for electrochemical supercapacitors, Chem. Soc. Rev. 41 (2012) 797–828.
[8] C. Liu, F. Li, L.P. Ma, H.M. Cheng, Advanced materials for energy storage, Adv. Mater. 22 (2010).
[9] P.J. Hall, M. Mirzaeian, S.I. Fletcher, F.B. Sillars, A.J. Rennie, G.O. Shitta-Bey, G. Wilson, A. Cruden, R. Carter, Energy storage in electrochemical capacitors: designing functional materials to improve performance, Energy Environ. Sci. 3 (2010) 1238–1251.
[10] V. Augustyn, P. Simon, B. Dunn, Pseudocapacitive oxide materials for high-rate electrochemical energy storage, Energy Environ. Sci. 7 (2014) 1597–1614.
[11] P. Simon, Y. Gogotsi, B. Dunn, Where do batteries end and supercapacitors begin?, Science 343 (2014) 1210–1211.
[12] X. Lang, A. Hirata, T. Fujita, M. Chen, Nanoporous metal/oxide hybrid electrodes for electrochemical supercapacitors, Nat. Nanotechnol. 6 (2011) 232–236.
[13] J. Jiang, Y. Li, J. Liu, X. Huang, C. Yuan, X.W.D. Lou, Recent advances in metal oxide-based electrode architecture design for electrochemical energy storage, Adv. Mater. 24 (2012) 5166–5180.
[14] Y. Zeng, M. Yu, Y. Meng, P. Fang, X. Lu, Y. Tong, Iron-based supercapacitor electrodes: advances and challenges, Adv. Energy Mater. (2016).
[15] W. Wei, X. Cui, W. Chen, D.G. Ivey, Manganese oxide-based materials as electrochemical supercapacitor electrodes, Chem. Soc. Rev. 40 (2011) 1697–1721.
[16] T. Cottineau, M. Toupin, T. Delahaye, T. Brousse, D. Belanger, Nanostructured transition metal oxides for aqueous hybrid electrochemical supercapacitors, Appl. Phys. A 82 (2006) 599–606.
[17] J. Shen, J. Wu, L. Pei, M.T.F. Rodrigues, Z. Zhang, F. Zhang, X. Zhang, P.M. Ajayan, M. Ye, $CoNi_2S_4$-graphene-2D-$MoSe_2$ as an advanced electrode material for supercapacitors, Adv. Energy Mater. (2016).
[18] J. Yang, C. Yu, X. Fan, S. Liang, S. Li, H. Huang, Z. Ling, C. Hao, J. Qiu, Electroactive edge site-enriched nickel–cobalt sulfide into graphene frameworks for high-performance asymmetric supercapacitors, Energy Environ. Sci. 9 (2016) 1299–1307.

[19] J. Zhao, J. Chen, S. Xu, M. Shao, Q. Zhang, F. Wei, J. Ma, M. Wei, D.G. Evans, X. Duan, Hierarchical nimn layered double hydroxide/carbon nanotubes architecture with superb energy density for flexible supercapacitors, Adv. Funct. Mater. 24 (2014) 2938–2946.
[20] H. Jiang, T. Zhao, C. Li, J. Ma, Hierarchical self-assembly of ultrathin nickel hydroxide nanoflakes for high-performance supercapacitors, J. Mater. Chem. 21 (2011) 3818–3823.
[21] Y. Yu, S.-Y. Huang, Y. Li, S.N. Steinmann, W. Yang, L. Cao, Layer-dependent electrocatalysis of MoS_2 for hydrogen evolution, Nano Lett. 14 (2014) 553–558.
[22] J. Yang, C. Yu, X. Fan, C. Zhao, J. Qiu, Ultrafast self-assembly of graphene oxide-induced monolithic NiCo–carbonate hydroxide nanowire architectures with a superior volumetric capacitance for supercapacitors, Adv. Funct. Mater. 25 (2015) 2109–2116.
[23] M. Zhi, C. Xiang, J. Li, M. Li, N. Wu, Nanostructured carbon–metal oxide composite electrodes for supercapacitors: a review, Nanoscale 5 (2013) 72–88.
[24] H. Jiang, J. Ma, C. Li, Mesoporous carbon incorporated metal oxide nanomaterials as supercapacitor electrodes, Adv. Mater. 24 (2012) 4197–4202.
[25] R. Rakhi, H.N. Alshareef, Enhancement of the energy storage properties of supercapacitors using graphene nanosheets dispersed with metal oxide-loaded carbon nanotubes, J. Power Sources 196 (2011) 8858–8865.
[26] R. Rakhi, D. Cha, W. Chen, H.N. Alshareef, Electrochemical energy storage devices using electrodes incorporating carbon nanocoils and metal oxides nanoparticles, J. Phys. Chem. C. 115 (2011) 14392–14399.
[27] X. Chia, A.Y.S. Eng, A. Ambrosi, S.M. Tan, M. Pumera, Electrochemistry of nanostructured layered transition-metal dichalcogenides, Chem. Rev. 115 (2015) 11941–11966.
[28] M. Sun, H. Liu, J. Qu, J. Li, Earth-rich transition metal phosphide for energy conversion and storage, Adv. Energy Mater. (2016) 1600087.
[29] L. Shen, J. Wang, G. Xu, H. Li, H. Dou, X. Zhang, $NiCo_2S_4$ nanosheets grown on nitrogen-doped carbon foams as an advanced electrode for supercapacitors, Adv. Energy Mater. 5 (2015) 1400977.
[30] J. Xiao, L. Wan, S. Yang, F. Xiao, S. Wang, Design hierarchical electrodes with highly conductive $NiCo_2S_4$ nanotube arrays grown on carbon fiber paper for high-performance pseudocapacitors, Nano Lett. 14 (2014) 831–838.
[31] C. Xia, Q. Jiang, C. Zhao, P.M. Beaujuge, H.N. Alshareef, Asymmetric supercapacitors with metal-like ternary selenides and porous graphene electrodes, Nano Energy 24 (2016) 78–86.
[32] J.F. Callejas, C.G. Read, C.W. Roske, N.S. Lewis, R.E. Schaak, Synthesis, characterization, and properties of metal phosphide catalysts for the hydrogen-evolution reaction, Chem. Mater. 28 (2016) 6017–6044.
[33] X. Wang, H.-M. Kim, Y. Xiao, Y.-K. Sun, Nanostructured metal phosphide-based materials for electrochemical energy storage, J. Mater. Chem. A 4 (2016) 14915–14931.
[34] Y. Shi, B. Zhang, Recent advances in transition metal phosphide nanomaterials: synthesis and applications in hydrogen evolution reaction, Chem. Soc. Rev. 45 (2016) 1529–1541.
[35] W. Du, S. Wei, K. Zhou, J. Guo, H. Pang, X. Qian, One-step synthesis and graphene-modification to achieve nickel phosphide nanoparticles with electrochemical properties suitable for supercapacitors, Mater. Res. Bull. 61 (2015) 333–339.
[36] S. Duan, R. Wang, $Au/Ni_{12}P_5$ core/shell nanocrystals from bimetallic heterostructures: In situ synthesis, evolution and supercapacitor properties, NPG Asia Mater. 6 (2014) e122.
[37] H. Wu, Y. Ni, M. Wang, D. Lu, Shape-controlled synthesis and performance comparison of Ni_2P nanostructures, CrystEngComm 18 (2016) 5155–5163.
[38] Y. Lu, J.-k. Liu, X.-y. Liu, S. Huang, T.-q. Wang, X.-l. Wang, C.-d. Gu, J.-p. Tu, S.X. Mao, Facile synthesis of Ni-coated Ni_2P for supercapacitor applications, CrystEngComm 15 (2013) 7071–7079.
[39] T. Brousse, D. Bélanger, J.W. Long, To be or not to be pseudocapacitive?, J. Electrochem. Soc. 162 (2015) A5185–A5189.
[40] M.-C. Liu, L.-B. Kong, L. Kang, X. Li, F.C. Walsh, M. Xing, C. Lu, X.-J. Ma, Y.-C. Luo, Synthesis and characterization of $M_3V_2O_8$ (M = Ni or Co) based nanostructures: a new family of high performance pseudocapacitive materials, J. Mater. Chem. A 2 (2014) 4919–4926.
[41] J. Yang, X. Duan, Q. Qin, W. Zheng, Solvothermal synthesis of hierarchical flower-like β-NiS with excellent electrochemical performance for supercapacitors, J. Mater. Chem. A 1 (2013) 7880–7884.
[42] T.-W. Lin, C.-S. Dai, K.-C. Hung, High energy density asymmetric supercapacitor based on $NiOOH/Ni_3S_2$/3D graphene and Fe_3O_4/graphene composite electrodes, Sci. Rep. 4 (2014) 7274.
[43] Y. Liu, R. Wang, X. Yan, Synergistic effect between ultra-small nickel hydroxide nanoparticles and reduced graphene oxide sheets for the application in high-performance asymmetric supercapacitor, Sci. Rep. 5 (2015) 11095.
[44] X. Chen, M. Cheng, D. Chen, R. Wang, Shape-controlled synthesis of Co_2P nanostructures and their application in supercapacitors, ACS Appl. Mater. Interfaces 8 (2016) 3892–3900.
[45] R. Rakhi, W. Chen, D. Cha, H.N. Alshareef, Substrate dependent self-organization of mesoporous cobalt oxide nanowires with remarkable pseudocapacitance, Nano Lett. 12 (2012) 2559–2567.
[46] R. Ren, M.S. Faber, R. Dziedzic, Z. Wen, S. Jin, S. Mao, J. Chen, Metallic CoS_2 nanowire electrodes for high cycling performance supercapacitors, Nanotechnology 26 (2015) 494001.
[47] G. Zhang, X.W.D. Lou, General solution growth of mesoporous $NiCo_2O_4$ nanosheets on various conductive substrates as high-performance electrodes for supercapacitors, Adv. Mater. 25 (2013) 976–979.
[48] G. Kresse, D. Joubert, From ultrasoft pseudopotentials to the projector augmented-wave method, Phys. Rev. B 59 (1999) 1758.
[49] P.E. Blöchl, O. Jepsen, O.K. Andersen, Improved tetrahedron method for brillouin-zone integrations, Phys. Rev. B 49 (1994) 16223.
[50] H. Liang, A.N. Gandi, D.H. Anjum, X. Wang, U. Schwingenschlögl, H.N. Alshareef, Plasma-assisted synthesis of NiCoP for efficient overall water splitting, Nano Lett. 16 (2016) 7718–7725.
[51] P.E. Blanchard, A.P. Grosvenor, R.G. Cavell, A. Mar, X-ray photoelectron and absorption spectroscopy of metal-rich phosphides M_2P and M_3P (M = Cr–Ni), Chem. Mater. 20 (2008) 7081–7088.
[52] M. Ledendecker, S. Krick Calderón, C. Papp, H.P. Steinrück, M. Antonietti, M. Shalom, The synthesis of nanostructured Ni_5P_4 films and their use as a non-noble bifunctional electrocatalyst for full water splitting, Angew. Chem. Int. Ed. 54 (2015) 12361–12365.
[53] N. Spinner, W.E. Mustain, Effect of nickel oxide synthesis conditions on its physical properties and electrocatalytic oxidation of methanol, Electrochim. Acta 56 (2011) 5656–5666.
[54] H. Bode, K. Dehmelt, J. Witte, Zur kenntnis der nickelhydroxidelektrode—I. Über das nickel (II)-hydroxidhydrat, Electrochim. Acta 11 (1966) 1079–1081.
[55] D. Singh, Characteristics and effects of γ-NiOOH on cell performance and a method to quantify it in nickel electrodes, J. Electrochem. Soc. 145 (1998) 116–120.
[56] K. Provazi, M. Giz, L. Dall'Antonia, S.C. de Torresi, The effect of Cd, Co, and Zn as additives on nickel hydroxide opto-electrochemical behavior, J. Power Sources 102 (2001) 224–232.
[57] J. Chen, D. Bradhurst, S. Dou, H.K. Liu, Nickel hydroxide as an active material for the positive electrode in rechargeable alkaline batteries, J. Electrochem. Soc. 146 (1999) 3606–3612.
[58] T. Uchikoshi, Y. Sakka, M. Yoshitake, K. Yoshihara, A study of the passivating oxide layer on fine nickel particles, Nanostruct. Mater. 4 (1994) 199–206.
[59] N. McIntyre, M. Cook, X-ray photoelectron studies on some oxides and hydroxides of cobalt, nickel, and copper, Anal. Chem. 47 (1975) 2208–2213.
[60] H. Liang, L. Li, F. Meng, L. Dang, J. Zhuo, A. Forticaux, Z. Wang, S. Jin, Porous two-dimensional nanosheets converted from layered double hydroxides and their applications in electrocatalytic water splitting, Chem. Mater. 27 (2015) 5702–5711.
[61] K. Kim, N. Winograd, X-ray photoelectron spectroscopic studies of nickel-oxygen surfaces using oxygen and argon ion-bombardment, Surf. Sci. 43 (1974) 625–643.
[62] X. Yang, J. Zhu, L. Qiu, D. Li, Bioinspired effective prevention of restacking in multilayered graphene films: towards the next generation of high-performance supercapacitors, Adv. Mater. 23 (2011) 2833–2838.
[63] Y. Zhang, B. Wang, F. Liu, J. Cheng, X.-w. Zhang, L. Zhang, Full synergistic contribution of electrodeposited three-dimensional $NiCo_2O_4$@MnO_2 nanosheet networks electrode for asymmetric supercapacitors, Nano Energy 27 (2016) 627–637.
[64] X. Yu, B. Lu, Z. Xu, Super long-life supercapacitors based on the construction of nanohoneycomb-like strongly coupled $CoMoO_4$–3D graphene hybrid electrodes, Adv. Mater. 26 (2014) 1044–1051.
[65] X.-F. Lu, D.-J. Wu, R.-Z. Li, Q. Li, S.-H. Ye, Y.-X. Tong, G.-R. Li, Hierarchical $NiCo_2O_4$ nanosheets@hollow microrod arrays for high-performance asymmetric supercapacitors, J. Mater. Chem. A 2 (2014) 4706–4713.
[66] W. Kong, C. Lu, W. Zhang, J. Pu, Z. Wang, Homogeneous core–shell $NiCo_2S_4$ nanostructures supported on nickel foam for supercapacitors, J. Mater. Chem. A 3 (2015) 12452–12460.

Hanfeng Liang received his PhD in applied chemistry in 2015 from Xiamen University. As a visiting graduate student, he studied at University of Wisconsin-Madison from 2013 to 2015. He is currently a postdoc in Prof. Husam N. Alshareef's group at KAUST. His current research focuses on earth-abundant materials for electrocatalysis, sodium-ion batteries, and supercapacitors.

Chuan Xia is currently a PhD candidate in the Materials Science and Engineering program at KAUST. His research interests focus on the development of nanostructured chalcogenides and their applications.

Qiu Jiang obtained his bachelor degree from University of Science and Technology of China. He is currently a PhD student in the Materials Science and Engineering program at KAUST. His research interests focus on fabricating on-chip energy storage devices employing direct write and conventional lithography techniques.

Appala Naidu Gandi is a Postdoctoral fellow in the Physical Science and Engineering Division of King Abdullah University of Science and Technology. He received doctorate degree from the Imperial College London. He uses first-principles methods for studying various properties of materials. His main focus is on thermoelectric materials and lattice dynamics.

Udo Schwingenschlögl is a Professor in the Physical Science and Engineering Division of King Abdullah University of Science and Technology. He received diploma and doctorate degrees from the University of Augsburg. His research encompasses work across the fields of materials science, physics, and mathematics, with a strong focus on interdisciplinary questions.

Husam N. Alshareef is a Professor of Materials Science & Engineering at King Abdullah University of Science & Technology (KAUST). He obtained his PhD at North Carolina State University, USA. Following nearly 10 years of experience in the semiconductor industry, he joined KAUST in 2009. His group is interested in developing semiconductor nanomaterials for electronics and energy applications.